

# Noninvasive Imaging of PSMA in Prostate Tumors with $^{89}\text{Zr}$ -Labeled huJ591 Engineered Antibody Fragments: The Faster Alternatives

Nerissa Therese Viola-Villegas,<sup>†</sup> Kuntal K. Sevak,<sup>†</sup> Sean D. Carlin,<sup>†</sup> Michael G. Doran,<sup>†</sup> Henry W. Evans,<sup>†</sup> Derek W. Bartlett,<sup>‡</sup> Anna M. Wu,<sup>\*,§</sup> and Jason S. Lewis<sup>\*,†</sup>

<sup>†</sup>Department of Radiology and the Program in Molecular Pharmacology and Chemistry, Memorial Sloan Kettering Cancer Center, 1275 York Avenue, New York, New York 10065, United States

<sup>‡</sup>ImaginAb, Inc., 423 Hindry Avenue, Suite D, Inglewood, California 90301, United States

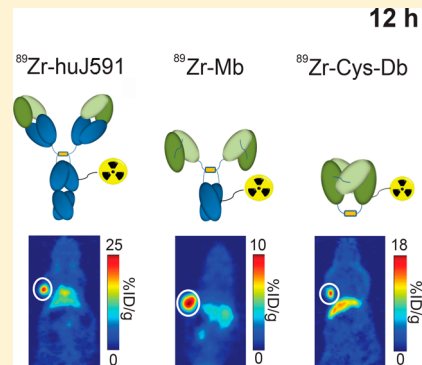
<sup>\*</sup>Department of Molecular and Medical Pharmacology, Crump Institute for Molecular Medicine, David Geffen School of Medicine at UCLA, 700 Westwood Plaza, Los Angeles, California 90095, United States

## S Supporting Information

**ABSTRACT:** Engineered antibody fragments offer faster delivery with retained tumor specificity and rapid clearance from nontumor tissues. Here, we demonstrate that positron emission tomography (PET) based detection of prostate specific membrane antigen (PSMA) in prostatic tumor models using engineered bivalent antibodies built on single chain fragments (scFv) derived from the intact antibody, huJ591, offers similar tumor delineating properties but with the advantage of rapid targeting and imaging.  $^{89}\text{Zr}$ -radiolabeled huJ591 scFv (dimeric scFv-C<sub>H</sub>3;  $^{89}\text{Zr}$ -Mb) and cysteine diabodies (dimeric scFv;  $^{89}\text{Zr}$ -Cys-Db) demonstrated internalization and similar  $K_{dS}$  ( $\sim 2$  nM) compared to  $^{89}\text{Zr}$ -huJ591 in PSMA(+) cells. Tissue distribution assays established the specificities of both  $^{89}\text{Zr}$ -Mb and  $^{89}\text{Zr}$ -Cys-Db for PSMA(+) xenografts ( $6.2 \pm 2.5\%$  ID/g and  $10.2 \pm 3.4\%$  ID/g at 12 h p.i. respectively), while minimal accumulation in PSMA(−) tumors was observed. From the PET images,  $^{89}\text{Zr}$ -Mb and  $^{89}\text{Zr}$ -Cys-Db exhibited faster blood clearance than the parent huJ591

while tumor-to-muscle ratios for all probes show comparable values across all time points. *Ex vivo* autoradiography and histology assessed the distribution of the probes within the tumor. Imaging PSMA-expressing prostate tumors with smaller antibody fragments offers rapid tumor accumulation and accelerated clearance; hence, shortened wait periods between tracer administration and high-contrast tumor imaging and lower dose-related toxicity are potentially realized.

**KEYWORDS:** PSMA, PET, minibody, Cys-diabody, huJ591



Prostate cancer (PC) is one of the leading causes of cancer mortality in men in the US. Standard diagnostic screenings, which include digital rectal exam (DRE) and serum-based prostate specific antigen (PSA) assays, suffer from low sensitivity in early detection assessments, and additional tools are needed to improve staging and discriminate low- vs high-risk PC patients. Molecularly targeted imaging probes can address some of these limitations by providing a quantitative yet noninvasive approach, generating lesion maps necessary to select cancerous growths for biopsy and staging. Several PET agents are currently under investigation in the clinic for PC detection.  $^{18}\text{F}$ [FDG], the general gold standard for identifying malignant lesions via deregulated metabolism, inadequately marks PC stemming from low glucose consumption of primary tumors.<sup>1</sup> Other tracers such as  $^{18}\text{F}$ NaF are surrogates of more advanced disease, particularly metastatic bone deposits secondary to PC.<sup>2</sup> Choline-based  $^{18}\text{F}$  and  $^{11}\text{C}$  radiotracers showed moderate benefit in lymph node staging of PC patients,<sup>3</sup> but drawbacks arose due to limited sensitivity (>5 mm tumor size) as well as low specificity in differentiating benign disease (i.e., prostatitis) from malignant lesions.<sup>4,5</sup>

Androgen receptor activity can be probed using a radio-fluorinated analogue of dihydroxytestosterone, [ $^{18}\text{F}$ ]FDHT,<sup>6–8</sup> however, PC heterogeneity excludes the detection of malignancies that are resistant to hormone therapy, limiting the sensitivity of this imaging probe.<sup>6</sup>

The emergence of antibody-based carriers of therapeutic and diagnostic payloads presents a promising alternative delivery platform to biomarkers expressed on tumor cell surface as monoclonal antibodies (mAbs) possess high specificity to their targets. One such malignant marker is prostate specific membrane antigen (PSMA). This transmembrane protein is upregulated in the epithelium of prostatic cancer as well as in the neovasculature of melanoma and carcinoma of the stomach, kidney, bladder, lung, breast, colon, and pancreas.<sup>9–12</sup> Efforts to

**Special Issue:** Positron Emission Tomography: State of the Art

**Received:** February 26, 2014

**Revised:** April 21, 2014

**Accepted:** April 29, 2014

**Published:** April 29, 2014

target and delineate PSMA-expressing tumors using mAbs as vectors have advanced in recent years. The scintigraphy-based probe  $^{111}\text{In}$ -7E11 is an anti-PSMA targeting antibody diagnostic agent approved by the FDA, with specificity for an intracellular epitope of the antigen;<sup>13</sup> however, issues arose as binding sites are exposed only following apoptosis or necrosis.<sup>14,15</sup> Bander and co-workers subsequently developed the IgG huJ591 mAb that targets an extracellular epitope of PSMA.<sup>16</sup> The high selectivity of huJ591 for the antigen motivated preclinical work exploiting this mAb as a companion PET diagnostic using  $^{89}\text{Zr}$  ( $t_{1/2} \sim 78$  h, 909 keV).<sup>17</sup> In fact, the potential of  $^{89}\text{Zr}$ -huJ591 for delineating PSMA prostate tumor xenografts in small animal models set the foundation for clinical translation. Extended blood persistence is characteristic of most mAbs, warranting long waiting times (>1 day) between administration and optimal imaging contrast; thus, improvements on their pharmacokinetic (PK) profile are desired.

Previous findings have characterized smaller mAb derivatives, which offer rapid delivery and clearance from the bloodstream and normal tissues while retaining tumor-targeting properties of the parent antibody.<sup>18</sup> We rationalize that these smaller antibody fragments will address the underlying complications present in intact mAbs and are, thus, more suitable vectors for diagnostic applications. The minibody (Mb; scFv-C<sub>H</sub>3, ~80 kDa) and the cysteine-diabody (Cys-Db, Cys-modified scFv dimer, ~50 kDa) are two such antibody fragment platform formats that have been engineered with these principles in mind.<sup>19</sup> In this study, we explored the feasibility of using a PSMA-targeted Mb and Cys-Db as PET imaging probes with  $^{89}\text{Zr}$  as the radiometal of choice. By using these noncanonical antibody fragments, the goal is to establish the superior pharmacokinetics of these antibody fragments compared to huJ591 while maintaining tumor affinity and specificity to achieve same-day PET imaging.

## ■ EXPERIMENTAL SECTION

**Production of PSMA-Targeted Minibody and Cys-Diabody.** DNA sequences coding for the huJ591 variable regions were kindly provided by Dr. Neil Bander (Weill Cornell Medical College). The Mb (~80 kDa) is a bivalent homodimer with each monomer consisting of a single-chain variable fragment (scFv) linked to a human IgG1 hinge and C<sub>H</sub>3 domain. The Mb exists as a stable dimer due to the natural association between the C<sub>H</sub>3 domains as well as the formation of disulfide bonds within the hinge regions. The Cys-Db (~50 kDa) is a bivalent homodimer formed from two cross-paired scFv fragments. Each chain consists of the variable regions linked together by a Gly-Ser linker. A Cys tail, consisting of the sequence Gly-Gly-Cys, is fused to the C-terminus to enable the stabilization of the diabody complex by formation of a covalent disulfide bond. Purified huJ591 Mb and Cys-Db proteins were provided by ImaginAb, Inc. (Inglewood, CA).

**Protein Conjugation with Desferrioxamine.** A 3-fold equivalence of DFO-Bz-SCN (Macrocylics, Inc.) in DMSO (<5% total volume) was added to a solution of Mb or Cys-Db. huJ591 was reacted with DFO-Bz-SCN with a 1:5 mAb:chelate ratio. All reactions were incubated at 37 °C for 45 min with occasional mild stirring. Subsequent purification using a PD10 size exclusion column removed any unreacted DFO-Bz-SCN and DMSO with 0.9% saline as the mobile phase. The purified product was concentrated to a volume of ~500 μL using a Vivaspin 500 (MWCO: 10 kDa) centrifugal filter. SDS gel electrophoresis was performed to analyze purified DFO

conjugates of the Mb and Cys-Db (see the Supporting Information and SI Figure 1 in the Supporting Information).

**Radiolabeling Experiments with  $^{89}\text{Zr}$ .**  $^{89}\text{Zr}$ -oxalate (~37 MBq) was produced as previously described (see the Supporting Information).<sup>20</sup> The pH of  $^{89}\text{Zr}$  was adjusted to ~7.0–7.2 with 1 M Na<sub>2</sub>CO<sub>3</sub>. To each separate reaction, approximately 125–140 μg of Mb/Cys-Db-DFO (Mb-DFO, 1.56–1.75 nmol; Cys-Db-DFO, 2.5–2.8 nmol) or 250 μg (1.7 nmol) of huJ591-DFO was added and incubated at room temperature with intermittent mild shaking. After 1–1.5 h, the reaction was quenched with 10 μL of 50 mM DTPA (pH ~7) to remove any nonspecifically bound  $^{89}\text{Zr}$ . Crude radiolabeling yields were determined to be >95% using iTLC with the  $^{89}\text{Zr}$ -labeled proteins remaining close to the origin at  $R_f = 0.30$  while free Zr-89 is found near the solvent front at  $R_f = 0.65$ . Purification of  $^{89}\text{Zr}$ -proteins was performed using a PD10 size exclusion column with saline as the eluting buffer. The final radiochemical purity was >99% based on iTLC analysis. To address retained affinity for the antigen, both radiolabeled constructs  $^{89}\text{Zr}$ -Mb and  $^{89}\text{Zr}$ -Cys-Db were evaluated for immunoreactivity via a protocol established by Lindmo et al.<sup>21</sup>

**Cell Lines and Small Animal Xenografts.** LNCaP (PSMA(+)) and PC3 (PSMA(-)) human prostate cancer (PC) cell lines (American Type Culture Collection) were cultured in a sterile environment with 5% CO<sub>2</sub> at 37 °C and grown as described.<sup>22</sup>

All animal experiments were conducted in accordance with the guidelines set by MSKCC Animal Care and Use Committee and Research Animal Resource Center. For imaging experiments, male athymic nude (nu/nu) mice (6–8 week old, Taconic) were subcutaneously inoculated with dual tumors. LNCaP cells ( $3 \times 10^6$ ) in 1:1 medium:Matrigel (BD Sciences) were implanted on the left shoulder. PC3 cells ( $3 \times 10^6$  in 1:1 medium:Matrigel) were injected on the right shoulder. Tumor growth was monitored weekly and measured using vernier calipers with the volume calculated using the formula length × width × height × 0.52. Tumor volumes were allowed to reach 150–300 mm<sup>3</sup> prior to use.

**Internalization Assay.** Internalization of  $^{89}\text{Zr}$ -Mb,  $^{89}\text{Zr}$ -Cys-Db, and fully human  $^{89}\text{Zr}$ -huJ591 was investigated on LNCaP and PC3 cells. Approximately  $1 \times 10^5$  cells were seeded in a 12-well plate and incubated overnight. A volume of 2 mL of radiolabeled protein (37 kBq/mL) was added to each well. The plates were incubated at 37 and 4 °C for 0.5–24 h. Following each incubation period, the medium was collected and the cells were rinsed with 1 mL of phosphate buffered saline (PBS) twice. Surface-bound activity was collected by washing the cells in 1 mL of 100 mM acetic acid + 100 mM glycine (1:1, pH 3.5) at 4 °C. The adherent cells were then lysed with 1 mL of 1 M NaOH. Each wash was collected and counted for activity. The % internalized activity was calculated as the ratio of the activity of the lysate and the total activity from the medium, PBS, acid, and base washes.

**In Vitro Blocking Study.** In 12-well plates,  $1 \times 10^5$  LNCaP cells were seeded and incubated overnight to facilitate adherence. huJ591 (100 μg, 0.67 nmol) was either coadministered with the radioactive probes or preincubated for 1 h at 37 °C. After addition of  $^{89}\text{Zr}$ -Mb (1–2 μg, 12.5–25 pmol) and  $^{89}\text{Zr}$ -Cys-Db (1–2 μg, 20–40 pmol) in separate wells, the cells were incubated at 37 °C for 1 h and then carefully washed with medium to remove any excess unbound activity. Cells were lysed with 1 mL of 1 M NaOH and then measured for activity.

The level of bound radioligands was calculated as % bound, normalized to the amount of activity added.

**Saturation Binding Assay.** To determine the dissociation constant ( $K_d$ ) of each of the  $^{89}\text{Zr}$ -mAbs, saturation binding studies were conducted using LNCaP cells. Briefly, varying concentrations of the  $^{89}\text{Zr}$ -mAbs (0.03–3  $\mu\text{g}/\text{mL}$ , 0.2–60 pmol/mL) were added to  $5 \times 10^5$  cells in PBS containing 1% bovine serum albumin. The same experiment was repeated with additions of cold mAbs (140  $\mu\text{g}/\text{mL}$  for the Mb (1.75 nmol/mL) and Cys-Db (2.8 nmol/mL) and 300  $\mu\text{g}/\text{mL}$  for huJ591 (2 nmol/mL)) to determine nonspecific binding (NSB). After 1 h incubation at room temperature, the cells were washed twice with 1  $\times$  PBS. Specific binding (SB, nM), derived by subtracting NSB from total bound activity, was plotted against the amount of  $^{89}\text{Zr}$ -mAbs added. The dissociation constant,  $K_d$ , was calculated by nonlinear regression fitting of the resulting plot using GraphPad Prism v. 6.02. The study was conducted in duplicate.

**PET Imaging Experiments.** Mice ( $n = 3$ –4) bearing LNCaP xenografts were administered intravenously (iv) with 7.4–10.2 MBq of either  $^{89}\text{Zr}$ -Mb (28–38  $\mu\text{g}$ , 0.35–0.48 nmol) or  $^{89}\text{Zr}$ -Cys-Db (25–34  $\mu\text{g}$ , 0.50–0.68 nmol) in saline. The mice were anesthetized with 2% isoflurane in oxygen prior to imaging. Small-animal PET studies were conducted using microPET-R4 and Focus 120 scanners (Concorde Microsystems). PET images were acquired between 1 and 24 h after dose administration. Images were reconstructed via filter back projection. Using ASIPro VM software (Concorde Microsystems), volumes of interest (VOIs) were measured on various planar sections of the acquired image by manually drawing on the tumor site and on select organs. The mean VOI was calculated and expressed as % injected dose per gram of tumor tissue (% ID/g).

**Tissue Biodistribution Studies.** Single tumor bearing mice were administered intravenously with 370–555 kBq of either  $^{89}\text{Zr}$ -Mb (1–2  $\mu\text{g}$ , 12.5–25 pmol) or  $^{89}\text{Zr}$ -Cys-Db (1–2  $\mu\text{g}$ , 20–40 pmol). Competitive inhibition studies were performed with coadministration of ~200–500  $\mu\text{g}$  (2.5–10 nmol) of nonradioactive Mb or Cys-Db in LNCaP tumor-bearing mice ( $n = 3$ –5). In a separate cohort of mice ( $n = 4$ ) bearing the PSMA(+) tumor, the parent huJ591 (500  $\mu\text{g}$ , 3.3 nmol) was administered 36 h prior to dosing with  $^{89}\text{Zr}$ -Mb. Mice were euthanized by CO<sub>2</sub> asphyxiation after 1, 4, 12, and 24 h p.i. ( $n = 4$ –5 per group). Select tissues including the tumor were harvested and weighed with bound activity measured using a gamma counter (PerkinElmer). Activity measurements were background- and decay-corrected. The tissue uptake (% ID/g) was calculated against the total net activity injected.

**Autoradiography and Histology.** For autoradiographic studies, separate animals were administered with  $^{89}\text{Zr}$ -Mb,  $^{89}\text{Zr}$ -Cys-Db, and  $^{89}\text{Zr}$ -huJ591 (7.4–10.2 MBq) as described above, 24 h before sacrifice. Five minutes prior to sacrifice, animals were injected with Hoechst 33342 (1 mg/mL PBS, iv). Immediately following sacrifice, tumors were removed and frozen in OCT mounting medium (Sakura, Europe) and a series of 10  $\mu\text{m}$  tissue sections obtained. Autoradiographic distribution of  $^{89}\text{Zr}$  at 25  $\mu\text{m}$  pixel resolution was obtained by exposing the sections to a BAS MS2025 phosphor plate (FujiFilm), followed by reading on a GE Typhoon 7000IP plate reader. The same sections were then used to obtain high-magnification whole-mount images of Hoechst 33342 distribution and H&E staining as previously described.<sup>23</sup>

Following autoradiography, sections were fixed in 4% paraformaldehyde and stained for PSMA expression using rabbit anti-PSMA antibody (clone EPR6253, Abcam, 1:100 dilution) overnight at 4 °C, followed by goat anti-rabbit-Alexa-568 (Invitrogen, 1:100) for 1 h at room temperature. Sections were then imaged for Alexa-568 and Hoechst 33342 signals as previously described.<sup>24</sup> Finally, sections were stained with H&E, and digital microscopic images obtained in the same manner.

**Statistical Analysis.** Quantitative data were expressed as the mean  $\pm$  SD. Statistical analysis was performed using a one-way ANOVA test followed by Dunnett's multiple comparison test when applicable for biodistribution experiments. A two-tail Student's *t* test was employed in *in vitro* assays and tumor uptake comparison. A value of  $P < 0.05$  was considered statistically significant.

## RESULTS

**Characterization of  $^{89}\text{Zr}$ -Mb and  $^{89}\text{Zr}$ -Cys-Db.** Following production and purification of the Mb and Cys-Db, the proteins were analyzed to confirm their purity and identity prior to conjugation. The Mb and Cys-Db migrated primarily as covalent dimers of ~80 kDa and ~50 kDa, respectively, under nonreducing SDS-PAGE conditions, but migrated as monomers of ~40 kDa and ~25 kDa, respectively, under reducing SDS-PAGE conditions after disruption of the intermolecular disulfide bonds. A low level of product-related impurities (likely partially clipped fragments) of the Mb was also detected under the denaturing SDS-PAGE conditions. LC-TOF-MS confirmed the identity of the Mb and Cys-Db by molecular mass.

Facile DFO-Bz-SCN conjugation and  $^{89}\text{Zr}$ -radiolabeling of Mb, Cys-Db, and huJ591 were achieved. SDS-PAGE gel confirmed purity of both DFO-attached fragments compared to unmodified proteins (SI Figure 1 in the Supporting Information). Table 1 summarizes radiolabeling yield, purity,

**Table 1. Radiochemical and Immunoreactive Properties of  $^{89}\text{Zr}$ -Mb and  $^{89}\text{Zr}$ -Cys-Db**

	$^{89}\text{Zr}$ -Mb	$^{89}\text{Zr}$ -cys-Db
Immunoreactivity (%)	72.4 $\pm$ 1.7	72.8 $\pm$ 1.4
Specific Activity (mCi/mg)	7.2	8.1
Radiolabeling Yields (%)	>70	>70
Radiochemical Purity (%)	>99	>99

and specific activities of  $^{89}\text{Zr}$ -Mb and  $^{89}\text{Zr}$ -Cys-Db, which compared favorably to the previously reported values for  $^{89}\text{Zr}$ -huJ591.<sup>22</sup> Both  $^{89}\text{Zr}$ -Mb and  $^{89}\text{Zr}$ -Cys-Db demonstrated excellent radiolabeling yields (>70%) and radiochemical purities (>99%). Specific activities of 222–296 MBq/mg (17.8–23.7 MBq/ $\mu\text{mol}$ ) and 259–333 MBq/mg (12.9–16.6 MBq/ $\mu\text{mol}$ ) were attained for  $^{89}\text{Zr}$ -Mb ( $n = 8$ ) and  $^{89}\text{Zr}$ -Cys-Db ( $n = 5$ ) respectively. Both radiolabeled fragments sufficiently retained their affinity for PSMA with immunoreactivities established at ~72.4  $\pm$  1.7% for  $^{89}\text{Zr}$ -Mb and ~72.8  $\pm$  1.4% for  $^{89}\text{Zr}$ -Cys-Db ( $n = 3$  for each).

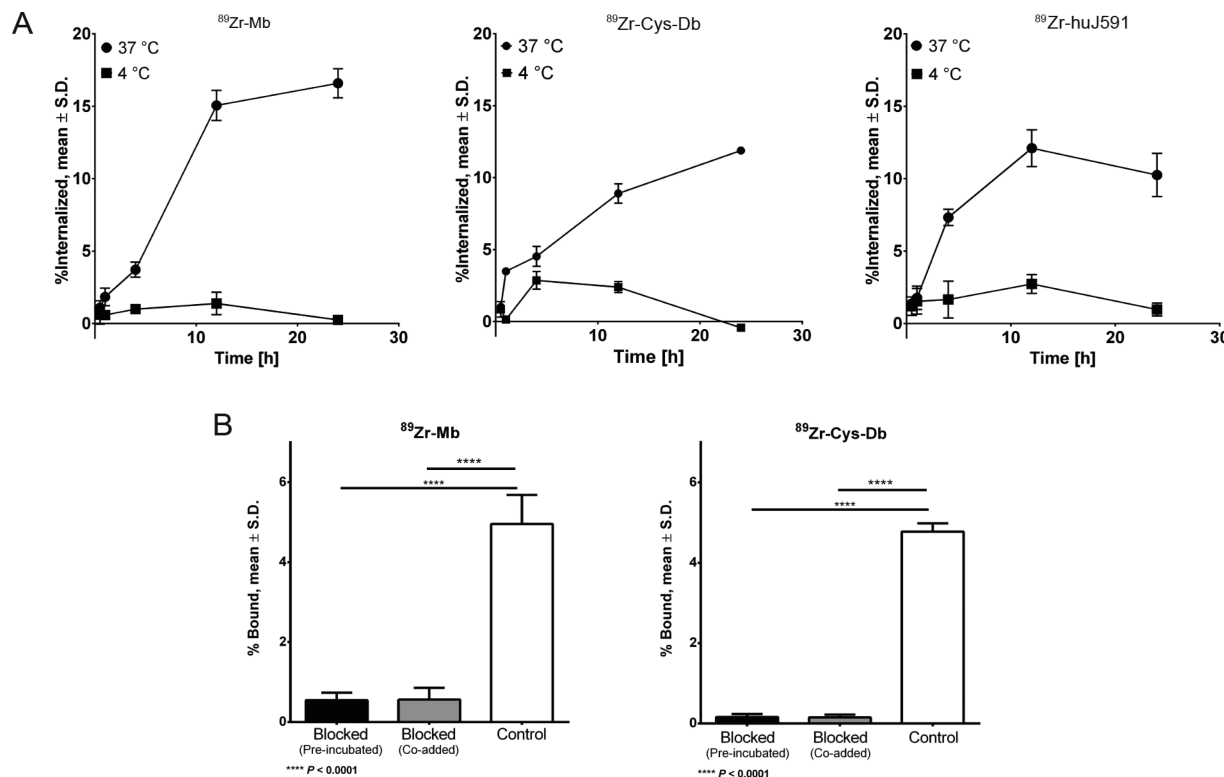


**Figure 1.** *In vitro* assays in LNCaP prostate cancer cells. Both antibody fragment radiotracers were added to LNCaP prostate cancer cells and incubated at 37 and 4 °C at 0.5, 1, 4, 12, and 24. (A) The internalization rates of <sup>89</sup>Zr-Mb (left) and <sup>89</sup>Zr-huJ591 (right) follow a nonlinear trend with slow uptake rates after 4 h of incubation; a subsequent increase in intracellular radioactivity with higher internalized fractions was observed for <sup>89</sup>Zr-Mb after 12 h. <sup>89</sup>Zr-Cys-Db (middle) displays a linear rate of internalization. All three radiotracers display minimal intracellular accumulation at all time periods at 4 °C. (B) In LNCaP prostate cancer cells, 1 h preincubation or coaddition of huJ591 (100 µg) with the radiotracer diminished binding of <sup>89</sup>Zr-Mb (1–2 µg, left) and <sup>89</sup>Zr-Cys-Db (1–2 µg, right).

**Variable *In Vitro* Internalization Rates of <sup>89</sup>Zr-Labeled huJ591, Mb, and Cys-Db.** With reports showing PSMA possessing a putative endocytic functionality,<sup>25,26</sup> we conducted *in vitro* internalization studies using LNCaP cells to compare the rates of internalization of <sup>89</sup>Zr-Mb, <sup>89</sup>Zr-Cys-Db, and <sup>89</sup>Zr-huJ591. The internalization patterns of all three radiotracers appear to be rapid, however, initial slow uptake was displayed by <sup>89</sup>Zr-Mb at 4 h at 37 °C with lower fractions internalized ( $3.7 \pm 0.5\%$ ,  $P = 0.002$ ) (Figure 1A, left panel). This was then followed by rapid internalization, peaking at 12 h with  $15.1 \pm 1.0\%$  ( $P = 0.027$ ), which reached a plateau at 24 h ( $16.6 \pm 1.0\%$ ). In Figure 1A (middle panel), <sup>89</sup>Zr-Cys-Db showed consistent linear internalization, spanning all time points ( $1.0 \pm 0.1\%$  at 0.5 h,  $3.5 \pm 0.2\%$  at 1 h,  $4.5 \pm 0.5\%$  at 4 h,  $8.9 \pm 0.7\%$  at 12 h, and  $11.9 \pm 0.1\%$  at 24 h) at 37 °C. At 37 °C, <sup>89</sup>Zr-huJ591 demonstrated internalization with  $1.4 \pm 0.1\%$  at 0.5 h,  $1.8 \pm 0.8\%$  at 1 h,  $7.3 \pm 0.6\%$  at 4 h,  $12.1 \pm 1.3\%$  at 12 h, and  $10.1 \pm 1.3\%$  at 24 h (Figure 1A, right panel). Minimal internalization was demonstrated by all three imaging probes at 4 °C, evidence of an endocytic uptake process.

**In Vitro Blocking Study of <sup>89</sup>Zr-Mb and <sup>89</sup>Zr-Cys-Db by huJ591.** The specificities of both <sup>89</sup>Zr-Mb and <sup>89</sup>Zr-Cys-Db to PSMA were evaluated by competitive inhibition with nonradioactive huJ591. In Figure 1B (left panel), <sup>89</sup>Zr-Mb demonstrated as much as  $4.96 \pm 0.73\%$  binding to LNCaP cells with no added huJ591. This level of bound Mb was satisfactorily blocked as much as 10-fold with both preincubated ( $0.55 \pm 0.19\%$ ,  $P < 0.0001$ ) and coadded ( $0.56 \pm 0.3\%$ ,  $P < 0.0001$ ) huJ591. Similar outcomes were observed

with <sup>89</sup>Zr-Cys-Db (Figure 1B, right panel) where, in the absence of huJ591, the radiotracer displayed  $4.77 \pm 0.21\%$  PSMA-binding activity; this uptake was significantly diminished by preincubation ( $0.16 \pm 0.08\%$ ,  $P < 0.0001$ ) and coaddition ( $0.15 \pm 0.07\%$ ,  $P < 0.0001$ ) of huJ591.

**Saturation Binding Assays.** <sup>89</sup>Zr-huJ591, <sup>89</sup>Zr-Mb, and <sup>89</sup>Zr-Cys-Db demonstrated specific binding and high affinities for PSMA localized on the surface of LNCaP cells. The saturation binding studies showed apparent  $K_d$  values that are similar for all three radiotracers: <sup>89</sup>Zr-huJ591 ( $K_d = 2.31 \pm 0.27$  nM), <sup>89</sup>Zr-Mb ( $K_d = 2.18 \pm 0.50$  nM), and <sup>89</sup>Zr-Cys-Db ( $K_d = 2.59 \pm 0.41$  nM).

**PSMA-Specific Tumor Uptake and Tissue Distribution of <sup>89</sup>Zr-Mb and <sup>89</sup>Zr-Cys-Db.** Tissue distributions of <sup>89</sup>Zr-Mb were analyzed in mice with single implants of PSMA(+) LNCaP (Figure 2A; SI Table 1 in the Supporting Information) or PSMA(−) PC3 tumors (SI Table 2 in the Supporting Information). Tumor uptake of <sup>89</sup>Zr-Mb at 1 h ( $2.3 \pm 0.5\%$  ID/g) was observed to steadily increase at 4 h p.i. ( $4.7 \pm 1.0\%$  ID/g). Accumulation of the probe in the tumor increased at 12 h p.i. with  $6.2 \pm 2.5\%$  ID/g and at 24 h p.i. ( $12.1 \pm 3.6\%$  ID/g). To establish the specificity of <sup>89</sup>Zr-Mb for PSMA *in vivo*, we performed blocking assays with various doses of nonradioactive Mb (SI Table 3 in the Supporting Information). At 12 h p.i., the uptake of <sup>89</sup>Zr-Mb was moderately decreased by 2-fold at 200 µg of coinjected cold Mb with  $3.73 \pm 1.27\%$  ID/g ( $P = 0.21$ ). Increasing the nonradioactive dose to ~500 µg did not significantly block the uptake either with  $3.82 \pm 0.70\%$  ID/g ( $P = 0.19$ ). We then employed huJ591 to block PSMA epitopes

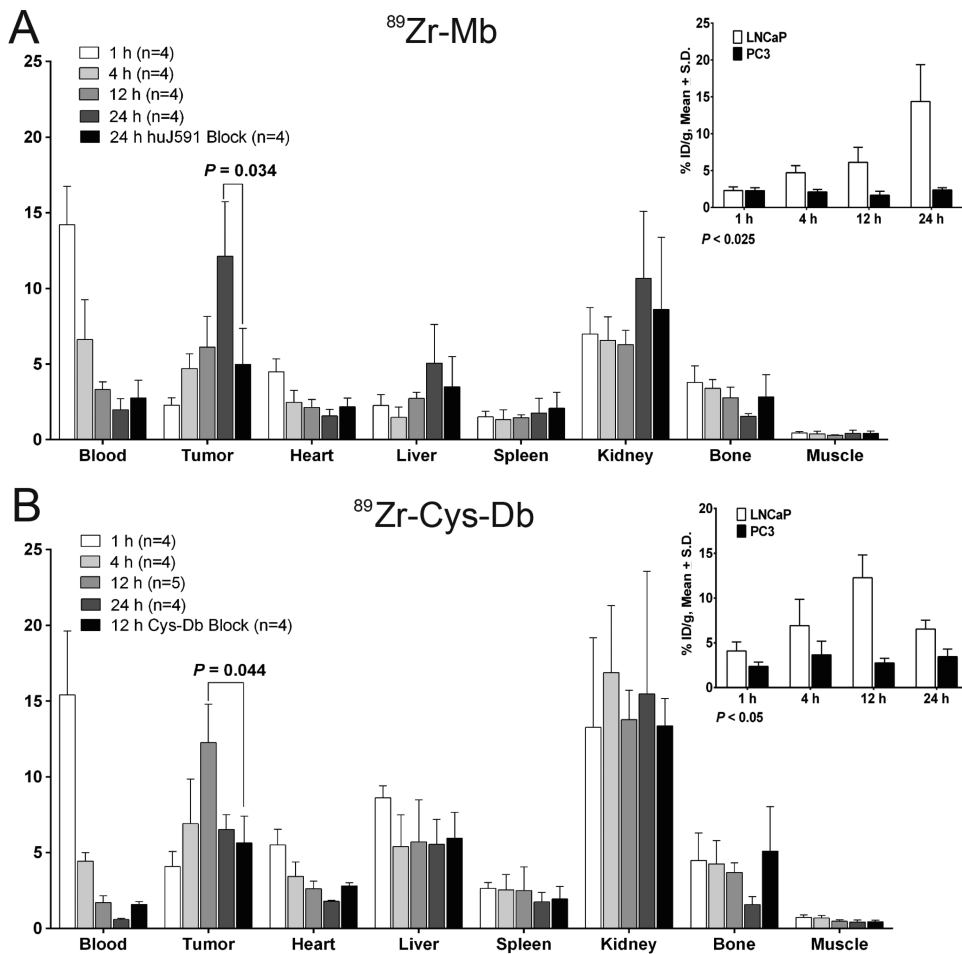


**Figure 2.** *Ex vivo* tissue distribution studies of <sup>89</sup>Zr-Mb and <sup>89</sup>Zr-Cys-Db administered intravenously in LNCaP (PSMA(+)) and PC3 (PSMA(-)) prostate tumor-bearing mice. (A) Biodistribution of <sup>89</sup>Zr-Mb at different time points (1–24 h) in select tissues including the tumor; a blocking dose of ~500 µg of huJ591 36 h prior to intravenous injection of <sup>89</sup>Zr-Mb effectively mitigated tumor uptake at 24 h p.i. (A, inset) Direct comparison between LNCaP and PC3 tumors displays cumulative <sup>89</sup>Zr-Mb uptake in the PSMA(+) xenograft, which was significantly higher as early as 4 h p.i., whereas nonspecific binding in the negative tumor is observed. (B) <sup>89</sup>Zr-Cys-Db exhibits selective tumor tissue targeting, which peaks at 12 h p.i. A blocking dose of 200 µg of nonradioactive Cys-Db decreases the radiotracer tumor uptake at 12 h p.i. (B, inset) Higher uptake of <sup>89</sup>Zr-Cys-Db in LNCaP tumors compared to PC3 implants at 12 and 24 h p.i. confirms the specificity of this imaging probe for PSMA.

required for binding. A 500 µg huJ591 dose was administered iv 36 h prior to injection of <sup>89</sup>Zr-Mb with the mice ( $n = 4$ ) euthanized 24 h p.i. of the radiotracer, which mitigated tumor uptake ( $5.0 \pm 2.4\% \text{ ID/g}$ ,  $P = 0.025$ ). The *in vivo* specificity of this probe was further strengthened with differences between <sup>89</sup>Zr-Mb accumulation in PSMA(−) PC3 tumors against LNCaP tumors in (Figure 2A, inset). The PC3 tumor sustained a constant accretion of  $2.3 \pm 0.4\% \text{ ID/g}$  at 1 h ( $P = 0.28$ ),  $2.1 \pm 0.3\% \text{ ID/g}$  at 4 h ( $P = 0.03$ ),  $1.7 \pm 0.5\% \text{ ID/g}$  at 12 h ( $P = 0.04$ ), and  $2.4 \pm 0.3\% \text{ ID/g}$  at 24 h. This nonspecific tumor uptake is attributed to the tumor's leaky vasculature.

Assessment of <sup>89</sup>Zr-Cys-Db localization in the PSMA(+) tumor demonstrated uptake with  $4.1 \pm 1.0\% \text{ ID/g}$  at 1 h,  $7.0 \pm 3.0\% \text{ ID/g}$  at 4 h, and  $12.3 \pm 2.5\% \text{ ID/g}$  at 12 h (Figure 2B; SI Table 4 in the Supporting Information). A decrease in tumor accretion at 24 h ( $6.5 \pm 1.0\% \text{ ID/g}$ ) was observed. Blocking with 200 µg of cold Cys-Db at 12 h p.i. effectively lowered the tumor accumulation to  $5.64 \pm 1.75\% \text{ ID/g}$  ( $P = 0.044$ ). PC3 tumor uptake (Figure 2B inset; SI Table 5 in the Supporting Information) displayed lower accretion across all time points with  $2.36 \pm 0.48\% \text{ ID/g}$  (1 h,  $P = 0.068$ ),  $3.65 \pm 1.54\% \text{ ID/g}$

(4 h,  $P = 0.12$ ),  $2.75 \pm 0.51\% \text{ ID/g}$  (12 h,  $P = 0.007$ ), and  $3.44 \pm 0.85\% \text{ ID/g}$  (24 h,  $P = 0.0011$ ).

**PSMA(+) Tumor Delineation.** We performed *in vivo* PET imaging in mice bearing PSMA(+) LNCaP tumors from 1 to 24 h on all three radiotracers (SI Figure 2 in the Supporting Information). In Figure 3A, planar sections of acquired images revealed accumulation of <sup>89</sup>Zr-Mb at 12 and 24 h p.i. Maximal intensity projection (MIP) at 12 h showed tumor delineation with nonspecific binding observed in the liver and kidneys. Similar results were achieved with <sup>89</sup>Zr-Cys-Db where localized delivery of the radiotracer to the tumor provided high contrasts at earlier time points (Figure 3B). In contrast to <sup>89</sup>Zr-huJ591 (Figure 3C), very minimal to no activity is present in the lung and heart in both <sup>89</sup>Zr-antibody fragments, proof that the circulating probes were eliminated faster than the intact mAb. Quantification of tumor uptake is presented in Figure 4A (SI Table 6 in the Supporting Information), which displays an increasing trend in tumor uptake for all three radiotracers. Tumor VOIs at 1 and 4 h p.i. were comparable. At 12 h p.i. the accumulation of both <sup>89</sup>Zr-Mb ( $6.85 \pm 0.87\% \text{ ID/g}$ ) and <sup>89</sup>Zr-Cys-Db ( $9.84 \pm 2.54\% \text{ ID/g}$ ) plateaued, whereas <sup>89</sup>Zr-huJ591 ( $15.84 \pm 1.79\% \text{ ID/g}$ ) steadily increased at 12 h p.i. After 24 h

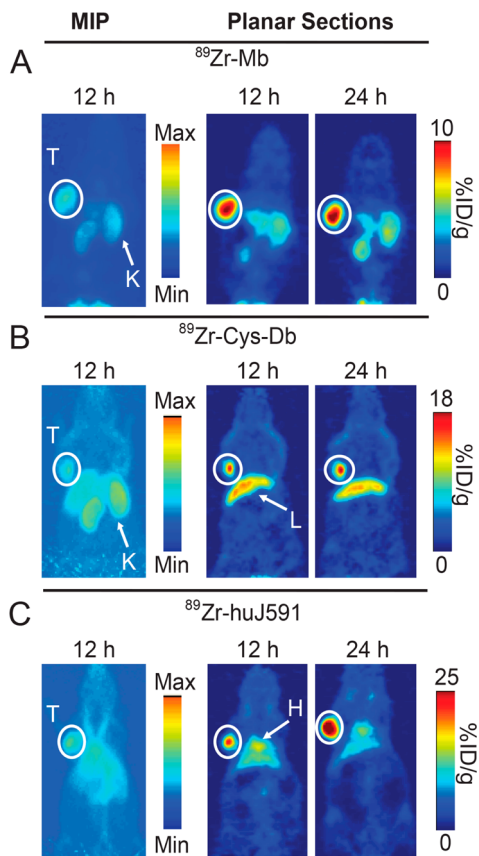


**Figure 3.** PET imaging. Representative maximum intensity projections (MIPs) and planar PET images of (A)  $^{89}\text{Zr}$ -Mb, (B)  $^{89}\text{Zr}$ -Cys-Db, and (C)  $^{89}\text{Zr}$ -huJ591 acquired in male athymic nude mice bearing LNCaP (left shoulder, T) prostate tumors xenografts at 12 and 24 h postinjection. Kidney (K) and liver (L) accumulations were observed for both  $^{89}\text{Zr}$ -Mb and  $^{89}\text{Zr}$ -Cys-Db and rationalized as routes of excretion. All three probes localize in the tumor, however, only  $^{89}\text{Zr}$ -huJ591 remains in circulation between 12 and 24 h.

p.i., the tumor uptake of the intact mAb was 3-fold higher compared to the scFv proteins. This lower tumor delivery of the engineered mAb fragments most likely stemmed from low availability of both fragments in the blood pool. As shown in the VOIs drawn on the heart (Figure 4B; SI Table 7 in the Supporting Information), a sharp decreasing trend in radiotracer activity was displayed by  $^{89}\text{Zr}$ -Cys-Db followed by  $^{89}\text{Zr}$ -Mb across all time points such that, at 12 h, only  $2.73 \pm 0.61\% \text{ ID/g}$   $^{89}\text{Zr}$ -Cys-Db and  $5.06 \pm 2.84\% \text{ ID/g}$   $^{89}\text{Zr}$ -Mb remained. At 24 h, residual cardiac activity from both tracers was determined (i.e.,  $2.00 \pm 0.18\% \text{ ID/g}$  for  $^{89}\text{Zr}$ -Cys-Db and  $3.26 \pm 1.20\% \text{ ID/g}$  for  $^{89}\text{Zr}$ -Mb).  $^{89}\text{Zr}$ -huJ591 heart activity remained consistently higher at all time points (i.e.,  $16.36 \pm 1.57\% \text{ ID/g}$  at 12 h and  $12.13 \pm 1.26\% \text{ ID/g}$  at 24 h).

Scrutiny of tumor-to-muscle (T/M) ratios from the PET scans disclosed no significant differences among all three radiotracers at all time points ( $P > 0.05$ ) (Figure 4C; SI Table 8 in the Supporting Information). Tumor-to-heart (T/H) ratios (Figure 4D; SI Table 9 in the Supporting Information) showed no distinctions between  $^{89}\text{Zr}$ -Mb and  $^{89}\text{Zr}$ -huJ591; however, analysis of T/H ratios for  $^{89}\text{Zr}$ -Cys-Db provided notably higher values at all time points against the intact mAb, for example,  $3.58 \pm 0.19$  vs  $0.98 \pm 0.19$  ( $P = 0.0002$ ) at 12 h and  $4.91 \pm 0.26$  vs  $2.22 \pm 0.46$  ( $P = 0.014$ ) at 24 h.

**Autoradiography and Histology.** Distribution of  $^{89}\text{Zr}$ -Mb (Figure 5A),  $^{89}\text{Zr}$ -Cys-Db (Figure 5B), and  $^{89}\text{Zr}$ -huJ591 (Figure 5C) at the microscopic level was evaluated using combined digital autoradiography (right panels) and whole-mount brightfield microscopy. The tumor tissues were viable with minimal necrosis observed as shown in the H&E stain (SI Figure 3a–c in the Supporting Information). PSMA expression (red stain, left panels) appeared to be essentially uniform in all LNCaP tumor sections examined. Binding was generally absent from regions of stromal infiltration. Slightly increased immunoreactivity was observed in tumor necrotic regions, but was assumed to represent nonspecific antibody binding. For each construct, focal uptake of  $^{89}\text{Zr}$  was observed in central tumor regions, with seemingly less around the tumor periphery. There was no accumulation in necrotic regions. Regions of high  $^{89}\text{Zr}$  uptake were generally centered on areas of high vascular perfusion (as indicated by Hoechst 33342 staining in blue, left panels). However, not all perfused regions, in particular those observed around the tumor rim, were associated with  $^{89}\text{Zr}$  uptake. It is possible that vascular integrity or “leakiness” may play a role in determining the distribution of the  $^{89}\text{Zr}$ -labeled constructs in this tumor model. This data may serve to indicate that the relative tumor distribution of each of the  $^{89}\text{Zr}$  constructs appears to be equivalent over the time course of these experiments.

## DISCUSSION

Here in this study, we developed PSMA-targeting PET imaging probes using antibody fragments of huJ591 as carriers. We rationalize that these smaller derivatives are necessary to enable lower dose exposures and faster imaging, which can potentially decrease the burden on prostate cancer patients. We opted to utilize  $^{89}\text{Zr}$  as the radionuclide of choice for labeling these fragments to provide a systematic and parallel comparison to huJ591-PET. These results demonstrated significantly improved PK attributes of both  $^{89}\text{Zr}$ -labeled antibody fragments with retained tumor targeting properties and shorter tracer clearance, thus rendering both probes as excellent markers of PSMA(+) cancer with the advantage of same-day imaging.

Facile conjugation of DFO-Bz-SCN and  $^{89}\text{Zr}$ -radiolabeling of Mb and Cys-Db were achieved with high radiochemical yields and purities and with minimal loss of immunoreactivities. Consistently high specific activities for both  $^{89}\text{Zr}$ -constructs were produced after numerous labeling experiments. For uniformity, huJ591 was also conjugated with DFO-Bz-SCN, which offers the benefit of shorter and more straightforward conjugation compared to an earlier protocol used by our group.<sup>22</sup> All three probes were shown to internalize albeit with varying kinetics underpinning the critical use of radiometals in labeling internalizing proteins to capitalize on longer retention within the tumor for better imaging contrasts. We further demonstrated the specificity of both  $^{89}\text{Zr}$ -Mb and  $^{89}\text{Zr}$ -Cys-Db by coaddition or prior incubation of cold huJ591 in LNCaP cells. We next asked whether the binding affinities of  $^{89}\text{Zr}$ -Mb and  $^{89}\text{Zr}$ -Cys-Db are comparable to  $^{89}\text{Zr}$ -huJ591. From our saturation binding assays, all radiolabeled proteins displayed comparable  $K_{d\text{s}}$ , supporting the hypothesis that smaller antibody platforms offer stable association to PSMA in a similar fashion to the parent mAb. Our observed affinities for all  $^{89}\text{Zr}$ -mAbs are within the range reported for huJ591 labeled with  $^{131}\text{I}$  ( $K_d = 1.83 \pm 1.21 \text{ nM}$ )<sup>27</sup> and  $^{111}\text{In}$  ( $K_d = 3 \text{ nM}$ ).<sup>28</sup> Two reports of new anti-PSMA antibody fragments were

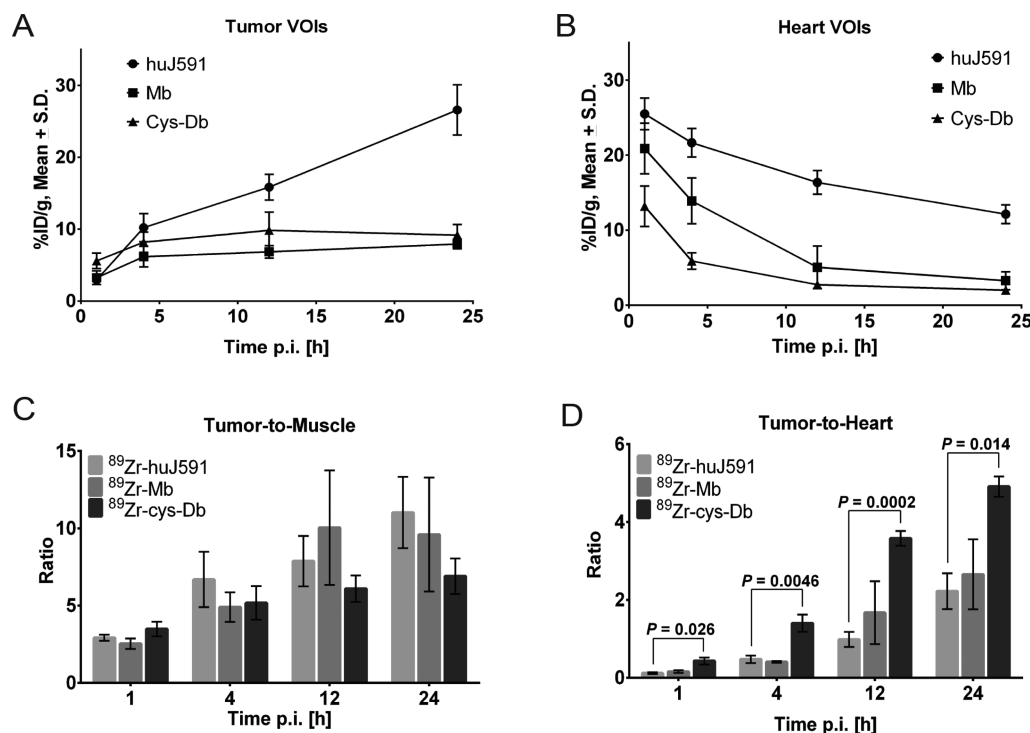


**Figure 4.** Time–activity curves of  $^{89}\text{Zr}$ -Mb,  $^{89}\text{Zr}$ -Cys-Db, and  $^{89}\text{Zr}$ -huJ591 demonstrating (A) tumor volumes of interest (VOIs), (B) blood clearance through heart VOIs, (C) tumor-to-muscle ratios, and (D) tumor-to-heart ratios from 1 to 24 h.

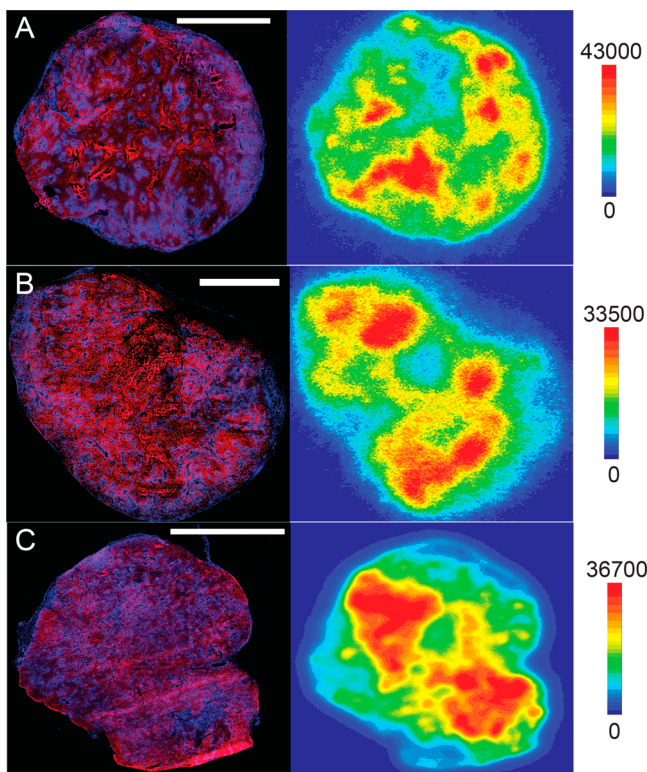


**Figure 5.** *Ex vivo* autoradiography and histology. Registered whole-mount micrographs of LNCaP tumor sections with PSMA staining (red) coregistered with Hoechst 33342 (blue) for perfusion (left) and digital autoradiography (right) of (A)  $^{89}\text{Zr}$ -Mb, (B)  $^{89}\text{Zr}$ -Cys-Db, and (C)  $^{89}\text{Zr}$ -huJ591. Bars = 2 mm.

recently published. Of particular interest is a diabody developed from the same parent huJ591 and labeled with  $^{99\text{m}}\text{Tc}$  ( $^{99\text{m}}\text{Tc}$ -huJ591Cdia) with a  $K_d$  of  $5.0 \pm 0.5 \text{ nM}$ .<sup>29</sup> Two chimeric scFv fragments derived from the parent murine mAb 3/F11 ( $K_d \sim 4.0 \text{ nM}$ ) established  $K_d$ s of  $8.3 \text{ nM}$  for D7-Fc and  $9.6 \text{ nM}$  for D7-CH3.<sup>30</sup> Moreover, a previous study investigating a single-chain variable fragment of another PSMA-targeting mAb, D2B, reported a 4-fold lower affinity ( $8.6 \text{ nM}$ ) via BIACore analysis,<sup>31</sup> thus rendering our antibody fragments potentially superior.

PET imaging visualized tumor uptake and rapid whole body clearance of the  $^{89}\text{Zr}$ -Mb and  $^{89}\text{Zr}$ -Cys-Db in murine xenografts. Tissue distribution studies showed minimal non-specific binding of both radiotracers in healthy tissues except in the hepatic and renal organs, which are routes of elimination.<sup>32</sup> This nonspecific binding observed for both liver and kidneys is significantly lower when compared to, for example,  $^{99\text{m}}\text{Tc}$ -huJ591Cdia with  $>13 \pm 1.8\% \text{ ID/g}$  and  $>29.2 \pm 3.5\% \text{ ID/g}$  respectively, albeit at 8 h p.i.<sup>29</sup> However, the uptake of our fragments, in particular,  $^{89}\text{Zr}$ -Cys-Db, in the liver and the kidneys is significantly lower. Retention of activity in the kidneys is likely due to a combination of clearance of the antibody fragments and radiolabeled metabolites, in addition to antigen-specific binding, as the proximal renal tubules have been reported to express PSMA,<sup>33</sup> only the latter would be reduced by blocking studies. Specific tumor delivery of both probes  $^{89}\text{Zr}$ -Cys-Db and  $^{89}\text{Zr}$ -Mb to PSMA was validated by addition of excess cold Cys-Db and huJ591 respectively. The competitive inhibition of  $^{89}\text{Zr}$ -Mb, however, was not straightforward with excess doses of Mb inefficiently attenuated. A plausible explanation can be attributed to the nonspecific clearance kinetics of each fragment, whereby competitive inhibition of the Mb should be examined at longer time periods (i.e., 24 h p.i.) when tumor uptake has stabilized. The results from autoradiography and histology (Figure 5B) reinforce this rationale as  $^{89}\text{Zr}$ -Mb was found to colocalize with

areas of vasculature even at 24 h p.i.; this, however, does not definitively discriminate between the vascular contributions of each construct. Stronger direct evidence is found in the blood activity at 12 and 24 h obtained from the *ex vivo* tissue distribution wherein accretion of  $^{89}\text{Zr}$ -Mb is 2-fold higher than that of the smaller  $^{89}\text{Zr}$ -Cys-Db. In addition, insufficient blocking of  $^{89}\text{Zr}$ -Mb at 12 h p.i. may likely stem from the fact that the internalization of PSMA is critically enhanced by ligand or antibody binding to the antigen.<sup>26,34,35</sup> As we have shown in our internalization assays, the kinetics vary with the minibody internalizing at a higher rate after 12 h p.i. With the PSMA recycling to the cell surface,<sup>35</sup> more binding sites are available for  $^{89}\text{Zr}$ -Mb delivery with ~3% ID/g circulating in the bloodpool.

In our study, engineered smaller fragments are postulated as viable imaging surrogates of therapeutic antibodies within the context of curtailing wait times between administration and imaging. Clear distinction between the three imaging probes is attained upon analysis of each tracer's *in vivo* pharmacokinetics due primarily to varying molecular size. Blood pool activity of all radiotracers demonstrated obvious disparities (Figure 4B) in clearance kinetics with  $^{89}\text{Zr}$ -Cys-Db clearly showing faster elimination during earlier time points.  $^{89}\text{Zr}$ -Mb showed parallel blood residencies at 12 and 24 h with  $^{89}\text{Zr}$ -Cys-Db while  $^{89}\text{Zr}$ -huJ591 still remained in circulation at higher activities after 24 h. Moreover, the measured tumor uptake from the PET images demonstrated significantly higher radiolocalization of  $^{89}\text{Zr}$ -huJ591 at later time points (i.e., 24 h). We ascribe this observation as a factor of systemic elimination of the fragments rather than loss of affinity. Intact mAbs possess innate prolonged blood residencies, significantly increasing its availability for tumor delivery. This extended circulation may benefit immunotherapies, but for diagnostic purposes, faster clearance with retained tumor localization is key to perform imaging within the same day of dosing. Faster blood pool clearance considerably enhances the image quality and resolution, which puts these  $^{89}\text{Zr}$ -engineered mAbs at a critical advantage. Moreover, the lower tumor delivery should not be taken as a major drawback as contrast or tumor-to-background ratios is considered one of the critical parameters not just in nuclear imaging but across all modalities. From the tumor-to-muscle ratios (Figure 4C), no significant disparities in contrast were observed between the antibody fragments and intact huJ591, supporting the notion that these intermediate-sized antibody fragments provide similar tumor delineating properties at the time points studied.

One of the benefits of using engineered fragments is arguably the lower dose toxicity due to shortened blood residencies and minimized nonspecific healthy tissue accumulation. Blood activities of both antibody fragments are far shorter than that of the intact huJ591 with residencies decreasing by 2-fold within 1–2 h postadministration. Thus, we surmise that, with such rapid kinetics, nontrivial absorbed whole body radioactive doses especially in hematopoietic tissues will be minimized proportionally. Certainly, with smaller antibody fragments, a radioisotope with a half-life matching the PK of the fragment (i.e.,  $^{64}\text{Cu}$ ,  $t_{1/2} = 12$  h) will afford better dosimetry profiles, especially if the probes are envisioned for repeat monitoring of treatment response in the same patient. Although immunoPET potentially holds a vital role in molecular and functional diagnosis, the lengthened circulation of intact antibodies and their nonspecific accumulation in normal tissues can impact radiotoxicity in normal organs, for example, the liver, the

spleen, and the rest of the hematopoietic system,<sup>36</sup> upon repeated PET scans. Careful dosimetry measurements are, therefore, necessary to limit patient exposure. We believe that the use of engineered fragments derived from the intact antibody provides such benefit and advantage with observed terminal half-lives of 3–11 h in mice and with maintained radiotracer target specificity.<sup>37</sup> Recognizing that imaging tools require rapid clearance of the probe at shorter time periods for optimum contrast and in order to minimize patient burden, the smaller Cys-Db and Mb fragments of huJ591 for PET imaging are obvious choices as companion diagnostics of PSMA-targeted therapy.

In summary, small engineered antibody fragments of huJ591 have high potential as alternative noninvasive imaging probes for the detection and staging of PSMA-positive prostate tumors. Both  $^{89}\text{Zr}$ -Mb and  $^{89}\text{Zr}$ -Cys-Db offer rapid tumor delineation and background clearance, essentially establishing these scFv-based antibody fragments as faster alternatives to the intact mAb.

## ASSOCIATED CONTENT

### S Supporting Information

Additional details of materials and methods; tables of data on biodistribution, competitive binding, tumor uptake, blood clearance of radiotracers, and tumor-to-muscle and tumor-to-blood ratios of radiotracers; and figures depicting SDS-PAGE gel electrophoresis, planar sections of serial PET images, and autoradiography and histology. This material is available free of charge via the Internet at <http://pubs.acs.org>.

## AUTHOR INFORMATION

### Corresponding Authors

\*(J.S.L.) Tel: (646)8883038. Fax: (646)8883059. E-mail: lewisj2@mskcc.org.

\*(A.M.W.) Tel: (310)7945088. Fax: (310)2068975. E-mail: awu@mednet.ucla.edu.

### Notes

The authors declare the following competing financial interest(s): DWB was an employee of ImaginAb, Inc.; AMW is a board member and consultant to ImaginAb, Inc.

## ACKNOWLEDGMENTS

Acknowledgments are extended to the Radiochemistry and Molecular Imaging Service Core and the grant-funding support provided by the NIH MSKCC Center Grant (P30-CA08748). This project was also funded in part with federal funds from the National Cancer Institute, National Institutes of Health, Department of Health and Human Services, under Contract No. HHSN261201100123C.

## REFERENCES

- (1) Lee, S. T.; Lawrentschuk, N.; Scott, A. M. PET in prostate and bladder tumors. *Semin. Nucl. Med.* **2012**, *42* (4), 231–46.
- (2) Fox, J. J.; Schoder, H.; Larson, S. M. Molecular imaging of prostate cancer. *Curr. Opin. Urol.* **2012**, *22* (4), 320–7.
- (3) Sanz, G.; Rioja, J.; Zudaire, J. J.; Berian, J. M.; Richter, J. A. PET and prostate cancer. *World J. Urol.* **2004**, *22* (5), 351–2.
- (4) Husarik, D. B.; Miralbell, R.; Dubs, M.; John, H.; Giger, O. T.; Gelet, A.; Cserenyak, T.; Hany, T. F. Evaluation of [(18)F]-choline PET/CT for staging and restaging of prostate cancer. *Eur. J. Nucl. Med. Mol. Imaging* **2008**, *35* (2), 253–63.
- (5) Brogsitter, C.; Zophel, K.; Kotzerke, J. 18F-Choline, 11C-choline and 11C-acetate PET/CT: comparative analysis for imaging prostate

- cancer patients. *Eur. J. Nucl. Mol. Imaging* **2013**, *40* (Suppl. 1), S18–27.
- (6) Dehdashti, F.; Picus, J.; Michalski, J. M.; Dence, C. S.; Siegel, B. A.; Katzenellenbogen, J. A.; Welch, M. J. Positron tomographic assessment of androgen receptors in prostatic carcinoma. *Eur. J. Nucl. Med. Mol. Imaging* **2005**, *32* (3), 344–50.
- (7) Beattie, B. J.; Smith-Jones, P. M.; Jhanwar, Y. S.; Schoder, H.; Schmidlein, C. R.; Morris, M. J.; Zanzonico, P.; Squire, O.; Meirerles, G. S.; Finn, R.; Namavari, M.; Cai, S.; Scher, H. I.; Larson, S. M.; Humm, J. L. Pharmacokinetic assessment of the uptake of 16beta-18F-fluoro-Salpha-dihydrotestosterone (FDHT) in prostate tumors as measured by PET. *J. Nucl. Med.* **2010**, *51* (2), 183–92.
- (8) Larson, S. M.; Morris, M.; Gunther, I.; Beattie, B.; Humm, J. L.; Akhurst, T. A.; Finn, R. D.; Erdi, Y.; Pentlow, K.; Dyke, J.; Squire, O.; Bornmann, W.; McCarthy, T.; Welch, M.; Scher, H. Tumor localization of 16beta-18F-fluoro-Salpha-dihydrotestosterone versus 18F-FDG in patients with progressive, metastatic prostate cancer. *J. Nucl. Med.* **2004**, *45* (3), 366–73.
- (9) Troyer, J. K.; Beckett, M. L.; Wright, G. L., Jr. Detection and characterization of the prostate-specific membrane antigen (PSMA) in tissue extracts and body fluids. *Int. J. Cancer* **1995**, *62* (5), 552–8.
- (10) Haffner, M. C.; Kronberger, I. E.; Ross, J. S.; Sheehan, C. E.; Zitt, M.; Muhlmann, G.; Ofner, D.; Zelger, B.; Ensinger, C.; Yang, X. J.; Geley, S.; Margreiter, R.; Bander, N. H. Prostate-specific membrane antigen expression in the neovasculature of gastric and colorectal cancers. *Hum. Pathol.* **2009**, *40* (12), 1754–61.
- (11) Milowsky, M. I.; Nanus, D. M.; Kostakoglu, L.; Sheehan, C. E.; Vallabhajosula, S.; Goldsmith, S. J.; Ross, J. S.; Bander, N. H. Vascular targeted therapy with anti-prostate-specific membrane antigen monoclonal antibody J591 in advanced solid tumors. *J. Clin. Oncol.* **2007**, *25* (5), 540–7.
- (12) Silver, D. A.; Pellicer, I.; Fair, W. R.; Heston, W. D.; Cordon-Cardo, C. Prostate-specific membrane antigen expression in normal and malignant human tissues. *Clin. Cancer Res.* **1997**, *3* (1), 81–5.
- (13) Chang, S. S.; Heston, W. D. The clinical role of prostate-specific membrane antigen (PSMA). *Urol. Oncol.* **2002**, *7* (1), 7–12.
- (14) Troyer, J. K.; Feng, Q.; Beckett, M. L.; Wright, G. L., Jr. Biochemical characterization and mapping of the 7E11-C5.3 epitope of the prostate-specific membrane antigen. *Urol. Oncol.* **1995**, *1* (1), 29–37.
- (15) Troyer, J. K.; Beckett, M. L.; Wright, G. L., Jr. Location of prostate-specific membrane antigen in the LNCaP prostate carcinoma cell line. *Prostate* **1997**, *30* (4), 232–42.
- (16) Liu, H.; Moy, P.; Kim, S.; Xia, Y.; Rajasekaran, A.; Navarro, V.; Knudsen, B.; Bander, N. H. Monoclonal antibodies to the extracellular domain of prostate-specific membrane antigen also react with tumor vascular endothelium. *Cancer Res.* **1997**, *57* (17), 3629–34.
- (17) Deri, M. A.; Zeglis, B. M.; Francesconi, L. C.; Lewis, J. S. PET imaging with (8)(9)Zr: from radiochemistry to the clinic. *Nucl. Med. Biol.* **2013**, *40* (1), 3–14.
- (18) Wu, A. M.; Yazaki, P. J.; Tsai, S.; Nguyen, K.; Anderson, A. L.; McCarthy, D. W.; Welch, M. J.; Shively, J. E.; Williams, L. E.; Raubitschek, A. A.; Wong, J. Y.; Toyokuni, T.; Phelps, M. E.; Gambhir, S. S. High-resolution microPET imaging of carcinoembryonic antigen-positive xenografts by using a copper-64-labeled engineered antibody fragment. *Proc. Natl. Acad. Sci. U.S.A.* **2000**, *97* (15), 8495–500.
- (19) Olafsen, T.; Cheung, C. W.; Yazaki, P. J.; Li, L.; Sundaresan, G.; Gambhir, S. S.; Sherman, M. A.; Williams, L. E.; Shively, J. E.; Raubitschek, A. A.; Wu, A. M. Covalent disulfide-linked anti-CEA diabody allows site-specific conjugation and radiolabeling for tumor targeting applications. *Protein Eng., Des. Sel.* **2004**, *17* (1), 21–7.
- (20) Holland, J. P.; Sheh, Y.; Lewis, J. S. Standardized methods for the production of high specific-activity zirconium-89. *Nucl. Med. Biol.* **2009**, *36* (7), 729–39.
- (21) Lindmo, T.; Boven, E.; Cuttitta, F.; Fedorko, J.; Bunn, P. A., Jr. Determination of the immunoreactive fraction of radiolabeled monoclonal antibodies by linear extrapolation to binding at infinite antigen excess. *J. Immunol. Methods* **1984**, *72* (1), 77–89.
- (22) Holland, J. P.; Divilov, V.; Bander, N. H.; Smith-Jones, P. M.; Larson, S. M.; Lewis, J. S. 89Zr-DFO-J591 for immunoPET of prostate-specific membrane antigen expression in vivo. *J. Nucl. Med.* **2010**, *51* (8), 1293–300.
- (23) Bartlett, R. M.; Beattie, B. J.; Naryanan, M.; Georgi, J. C.; Chen, Q.; Carlin, S. D.; Roble, G.; Zanzonico, P. B.; Gonen, M.; O'Donoghue, J.; Fischer, A.; Humm, J. L. Image-guided PO2 probe measurements correlated with parametric images derived from 18F-fluoromisonidazole small-animal PET data in rats. *J. Nucl. Med.* **2012**, *53* (10), 1608–15.
- (24) Oehler, C.; O'Donoghue, J. A.; Russell, J.; Zanzonico, P.; Lorenzen, S.; Ling, C. C.; Carlin, S. 18F-fluoromisonidazole PET imaging as a biomarker for the response to 5,6-dimethylxanthenone-4-acetic acid in colorectal xenograft tumors. *J. Nucl. Med.* **2011**, *52* (3), 437–44.
- (25) Rajasekaran, A. K.; Anilkumar, G.; Christiansen, J. J. Is prostate-specific membrane antigen a multifunctional protein? *Am. J. Physiol.* **2005**, *288* (5), C975–81.
- (26) Rajasekaran, S. A.; Anilkumar, G.; Oshima, E.; Bowie, J. U.; Liu, H.; Heston, W.; Bander, N. H.; Rajasekaran, A. K. A novel cytoplasmic tail MXXXXL motif mediates the internalization of prostate-specific membrane antigen. *Mol. Biol. Cell* **2003**, *14* (12), 4835–45.
- (27) Smith-Jones, P. M.; Vallabhajosula, S.; Goldsmith, S. J.; Navarro, V.; Hunter, C. J.; Bastidas, D.; Bander, N. H. In vitro characterization of radiolabeled monoclonal antibodies specific for the extracellular domain of prostate-specific membrane antigen. *Cancer Res.* **2000**, *60* (18), 5237–43.
- (28) McDevitt, M. R.; Barendswaard, E.; Ma, D.; Lai, L.; Curcio, M. J.; Sgouros, G.; Ballangrud, A. M.; Yang, W. H.; Finn, R. D.; Pellegrini, V.; Geerlings, M. W., Jr.; Lee, M.; Brechbiel, M. W.; Bander, N. H.; Cordon-Cardo, C.; Scheinberg, D. A. An alpha-particle emitting antibody ([213 Bi]J591) for radioimmunotherapy of prostate cancer. *Cancer Res.* **2000**, *60* (21), 6095–100.
- (29) Kampmeier, F.; Williams, J. D.; Maher, J.; Mullen, G. E.; Blower, P. J. Design and preclinical evaluation of a 99mTc-labelled diabody of mAb J591 for SPECT imaging of prostate-specific membrane antigen (PSMA). *EJNMMI Res.* **2014**, *4* (1), 13.
- (30) Wiehr, S.; Buhler, P.; Gierschner, D.; Wolf, P.; Rolle, A. M.; Keseneheimer, C.; Pichler, B. J.; Elsasser-Beile, U. Pharmacokinetics and PET imaging properties of two recombinant anti-PSMA antibody fragments in comparison to their parental antibody. *Prostate* **2014**, *74* (7), 743–55.
- (31) Frigerio, B.; Fracasso, G.; Luison, E.; Cingarlini, S.; Mortarino, M.; Coliva, A.; Seregni, E.; Bombardieri, E.; Zuccolotto, G.; Rosato, A.; Colombatti, M.; Canevari, S.; Figini, M. A single-chain fragment against prostate specific membrane antigen as a tool to build theranostic reagents for prostate cancer. *Eur. J. Cancer* **2013**, *49* (9), 2223–32.
- (32) Wu, A. M.; Senter, P. D. Arming antibodies: prospects and challenges for immunoconjugates. *Nat. Biotechnol.* **2005**, *23* (9), 1137–46.
- (33) Tasch, J.; Gong, M.; Sadelain, M.; Heston, W. D. A unique folate hydrolase, prostate-specific membrane antigen (PSMA): a target for immunotherapy? *Crit. Rev. Immunol.* **2001**, *21* (1–3), 249–61.
- (34) Liu, H.; Rajasekaran, A. K.; Moy, P.; Xia, Y.; Kim, S.; Navarro, V.; Rahmati, R.; Bander, N. H. Constitutive and antibody-induced internalization of prostate-specific membrane antigen. *Cancer Res.* **1998**, *58* (18), 4055–60.
- (35) Ghosh, A.; Heston, W. D. Tumor target prostate specific membrane antigen (PSMA) and its regulation in prostate cancer. *J. Cell. Biochem.* **2004**, *91* (3), 528–39.
- (36) Blumenthal, R. D.; Sharkey, R. M.; Snyder, D.; Goldenberg, D. M. Reduction by anti-antibody administration of the radiotoxicity associated with 131I-labeled antibody to carcinoembryonic antigen in cancer radioimmunotherapy. *J. Natl. Cancer Inst.* **1989**, *81* (3), 194–9.
- (37) McCabe, K. E.; Wu, A. M. Positive progress in immunoPET—not just a coincidence. *Cancer Biother. Radiopharm.* **2010**, *25* (3), 253–61.